防蝕工程　第十九卷第二期　第147～158頁　2005年6月
Journal of Chinese Corrosion Engineering, Vol.19 No.2, PP. 147~158 (2005)

銅合金在含氟環境中的兩種不同的破裂型態

陳彥羽、鄒仁江、張一熙、施漢章*

Two Distinct Fracture Modes of Copper Alloys in Fluoride Environments

Y. Y. Chen, R. J. Tzou, Y. S. Chang, H. C. Shih*

摘　要

本研究主要是利用慢速應變拉伸試驗來評估鋁黃銅與鋁青銅在含氟化物環境中，氟化物濃度與外加電位對這兩種銅合金其應力腐蝕破裂敏感性所造成的效應。實驗結果發現：鋁黃銅產生應力腐蝕的機制與去合金現象有關；而鋁青銅發生應力腐蝕的機制則是在某一範圍之外加電位下的鈍化膜剝落。對鋁黃銅來說，應力比與破裂時間比與氟離子濃度的對數值有很密切的關係。而鋁黃銅在其腐蝕電位的破裂型態是屬於延性撕裂狀的窩穴；另一方面，鋁青銅在過鈍態電位以上的破裂形式則是沿晶破裂。最後，本研究使用合金組成元素的微伽凡尼效應來估計兩種銅合金的陽極平衡電位。

關鍵詞：應力腐蝕破裂；鋁黃銅；鋁青銅；慢速應變拉伸試驗；窩穴；沿晶。

ABSTRACT

The susceptibility of aluminum brass and aluminum bronze to stress corrosion cracking (SCC) was evaluated in fluoride environments by means of the slow strain rate technique. The effects of fluoride concentration and applied electrochemical potential on the SCC susceptibility were investigated. The SCC mechanism of aluminum brass was found to be dependent upon the de-alloying phenomenon while that of aluminum bronze on the film rupture mechanism occurring within a certain range of applied electrochemical potentials. For aluminum brass, both the stress ratio and the time-to-fracture ratio were closely related to the logarithmic concentration of F^- ions. The fracture modes were ductile dimpled tearing fracture for the aluminum brass at the corrosion potential while intergranular for the aluminum bronze at various anodic potentials. The micro-galvanic effects of the constituent elements were used to estimate the anodic equilibrium potentials of the two alloys.

Keywords: Stress corrosion cracking; Aluminum brass; Aluminum bronze; Slow strain rate technique; Dimple; Intergranular.

國立清華大學材料科學與工程學系
Department of Materials Science and Engineering, National Tsing Hua University.
* 連絡作者(hcshih@mse.nthu.edu.tw)

1. Introduction

Several mechanisms for the stress corrosion cracking (SCC) of copper-based alloys have been proposed. Two that have found a wide acceptance are: (a) the mechano-chemical theory and (b) the de-alloying or selective dissolution theory. The mechano-chemical process includes the concept of passive film rupture / transient dissolution / repassivation. Under the action of tensile stress, the passive film, usually a metal oxide or a noble metal film that exists on a metal surface in a given environment, undergoes fracture. Unless the repair of these films is sufficiently rapid, metal dissolution occurs at the film fracture site, leading to crack initiation and propagation. Parkins[1] has developed a potentiodynamic method to predict the susceptibility of alloys to stress corrosion cracking failure in carbonate/bicarbonate solutions. Curves, resulting from the potentiodynamic polarization can provide a reasonably accurate prediction of the potential ranges, and of the kinetic factors controlling stress corrosion cracking. Such curves are well known to be a function of the rate at which the potential range is transversed, and use is made of this in the context of the SCC predictability.

Parker and Pearce [2] have suggested that SCC of alloys such as low alloy steels or copper alloys occurs under conditions of partial passivity such that general corrosion is inhibited but complete passivity of the metal surface is not attained. The potential regions showing partial passivity can be found by comparing fast and slow polarization scans. The test has the obvious advantage of being very quick. They also proposed that the susceptibility to cracking, and the form of cracking, are dependent upon the type of test being used. They concluded that the addition of phosphate ion in ammonium acetate solution inhibits both the crack initiation and propagation under constant strain conditions, but can cause SCC in constant strain rate tests.

The other theory that has gained wide acceptance suggests that de-alloying or selective dissolution of the alloying component, e.g. Zn in Cu-Zn alloys, is a contributory factor in the SCC process. In the case of Cu-Zn alloys, preferential dissolution of Zn occurs in the region of the crack tips, or at the grain boundaries [3, 4]. This leads to a porous Cu-rich matrix ahead of the crack tip, which is so mechanically unstable that ductile tearing may occur as a part of the overall cracking process. The equilibrium potential-pH diagram [5] for pure metals can be useful in predicting the susceptibility of de-alloying, and in evaluating the likelihood of certain electrochemical reactions taking place.

Torchio [6] and Mazza and Torchio [7] have found that a chloride-citrate solution can cause dezincification of aluminum brass. Torchio [8] also proposed that the acidic chloride solution can induce SCC of the aluminum brass, but he did not consider that de-alloying would reduce the aluminum content at the surface.

Finnegan et al. [9] have made use of the potential-pH diagram (Pourbaix diagram) to explain the dezincification of α-brass. Verink and Parrish [10] also applied the Pourbaix diagram to predict the denickelification of 90-10 cupronickel in chloride solutions. On the other hand, Shih et al. [11, 12] investigated the inhibiting effect of some inhibitors such as 1,2,3-benzotriazole (BTA) and 1,2,4-triazole for suppressing the SCC of 70-30 brass in chloride and in fluoride environments. The effects of pH, and electrochemical parameters such as pitting and protection potentials on the SCC of brass in fluoride solutions have been determined [13, 14].

This work is concerned about the mechanism of SCC of copper-based alloys in fluoride environments and attempts to manifest the validity of the theories in highlight of the above discussion.

2. Experimental Procedures

The chemical compositions (at%) of the copper-based alloys used in this study are as follows: (a) aluminum brass: 74.65% Cu, 21.19% Zn, 4.16% Al, and (b) aluminum bronze: 84.696% Cu, 13.03% Al, 2.27% Si, 0.004% Mn, as analyzed by the atomic emission spectrometer. Cylindrical SCC specimens were machined so that each was 50.8mm long and 5.08mm in diameter; they were threaded on both ends to facilitate the attachment to the pulling device and the gauge section was 3.175 mm in diameter and 12.7 mm in length, fabricated according to ASTM G49-85 [15]. Prior to the testing, the reduced area of the specimen in the tensile direction was polished using 400, 600, and 800 grit silicon carbide (SiC) papers, followed by a final polish using diamond paste on cloth to avoid any possible notch effects. The specimen was ultrasonically degreased by acetone, washed with distilled water, and finally dried in air.

Test solutions were prepared from reagent grade sodium fluoride (NaF, Merck), and de-ionized water to give concentrations in the range of 0.1N to 0.0001N at pH values varying from 6 to 7 in equilibrium with the atmosphere. All experiments were carried out at room temperature (~25℃).

The construction of the slow strain rate test (SSRT) apparatus used in this study has been described elsewhere [16]. The drive mechanism consisted of a moderately hard straining frame that produced six crosshead speeds adjusted by gear changes. The use of a constant speed motor drive in conjunction with a gearbox reducer and chain and sprockets gave a reliable positive drive system. Crosshead speeds lay between 5×10^{-4} and 5×10^{-6} mm/s.

The SSRT tests were carried out either under open-circuit conditions or under potentiostatic control using an AMEL MODEL 549-potentiostat. The test specimen passed through silicon rubber stoppers fitted at each end of a cylindrical glass test cell (200ml in volume), which contained the test solution. The cell contained an electrolytic bridge to an external SCE (saturated calomel electrode) and a platinum rod counter electrode for potential control. The load and elongation were measured continuously by a load cell and electrical dial gauge, respectively, the outputs of which were recorded on a computer-controlled X-Y recorder (YEW MODEL 3025) until fracture occurred. Bradford et al. [17-19] have found that in various SCC-inducing environments, cracking occurs in copper alloys only below a certain strain rate ($10^{-4}s^{-1}$) and, for this reason, a strain rate of $3.8\times10^{-6}s^{-1}$ was applied to the specimen in this study.
Electrochemical polarization tests were performed upon cylindrical specimens (10mm long, 5mm in diameter), cold mounted in epoxy resin to give an exposed area of 1 cm^2 to the solution. Before each experiment, the specimens were ground with emery paper up to 1500 grit, and polished with alumina powders (0.3 μm) to provide a mirror-like finish, then degreased by ultrasonic cleaning in acetone. The polarization apparatus was similar to a standard assembly used elsewhere [20, 21]. A potentiostat/galvanostat (EG&G Princeton Applied Research (PAR) Model 273) was used, and interfaced with an IBM PC/AT for data processing, storage, and analysis. The potentiodynamic measurements were carried out at both a high sweep rate of 1 V/min and a slow rate of 20 mV/min in the anodic (noble) direction. All the potential values given below are expressed on the standard hydrogen electrode (SHE) scale, which is 241 mV higher than the SCE. The total potential range scanned was 1.0V－from 0 V to 1.0 V.

After the experiments, SEM (HITACHI, S-4700, Type II), XRD (RIGAKU ME510-FM2), and EPMA (JEOL, JXA-8800M) were utilized for analyzing the fracture surfaces and the modes of SCC.

3. Results

3.1 Anodic polarizations

The potentiodynamic polarization curves in figure 1 show that aluminum brass is active over a wide range of fluoride concentrations from 10^{-1} to 10^{-4}N, and that the free corrosion potential, E_{corr}, which is at or slightly below +241 mV, is apparently independent of the fluoride concentration, [F^-]. This implies that the degree of polarization (or depolarization) at both the cathode and anode are approximately the same. The more concentrated fluoride ions yield higher anodic current densities for aluminum brass. However, aluminum bronze shows a distinct range of active-passive transition (~100 mV) at a scan rate of 20 mV/min, but remains entirely active at 1 V/min, as shown in figure 2. Irrespective of the scan rate, the E_{corr} of aluminum bronze is +191 mV in a solution of 0.1N NaF.

3.2 Effects of fluoride concentration

Engineering stress vs. strain curves were recorded for various fluoride concentrations either under the open-circuit potential conditions or at one of a range of controlled potentials. The SSRT was also conducted in air to provide a standard of comparison, because the strain rate has no appreciable effect on tensile stress or ductility in air [17]. This allowed calculation of two parameters： the time-to-fracture ratio (t_f) and the stress ratio (σ_R). The t_f value is defined as the ratio between the time-to-fracture in the test solution and the time-to-fracture in air. Similarly, the σ_f value is defined as the ratio between the stress at fracture in the test solution and the stress at fracture in air.

The results for aluminum brass at its free corrosion potential (+241 mV) are shown in figure 3. An apparent decrease in σ_R as well as t_f was observed with increasing fluoride concentration. The above results indicate that for aluminum brass, the higher the fluoride concentration, the greater the SCC susceptibility is. However, aluminum bronze showed no such behavior： both t_f and σ_R are independent of the fluoride concentration.

The linear regression with least squares fit for the curves in figure 3 correspond to the following empirical equations:

$$\sigma_R = -0.043 \log [F^-] + 0.645 \quad (1)$$

$$t_f = -0.069 \log [F^-] + 0.125 \quad (2)$$

where [F^-] is the fluoride concentration in units of N.

It is clear that aluminum brass suffers severe SCC in fluoride-containing environments, e.g. fracture within 2 h in a 10^{-1}N NaF solution. SCC susceptibility also can be seen in aluminum bronze, as shown in figure 4. There is a sudden drop in the σ_R value for aluminum bronze as the potential is increased from +341 mV to +391 mV, corresponding to the passive potential range of aluminum bronze (in 0.1N NaF). In other words, the SCC susceptibility for aluminum bronze starts to increase significantly in the passive range of potentials from +341 mV to +391 mV, and there is also susceptibility at potentials nobler than +391 mV, as clearly observed in the anodic polarization curve.

3.3 Fractographic examinations

The fracture surface of aluminum bronze shows predominantly intergranular stress corrosion cracking (IGSCC) at the anodic potential of +391 mV, as shown in figure 5(a). In addition, there are numerous pits and secondary cracks within the gauge length of the specimen, as shown in figure 5(b). The secondary stress corrosion cracks exhibited in figure 5(b) are mainly oriented in a direction perpendicular to the tensile axe (parallel to the fracture surface). Figure 5(c) shows the fracture surface along with the circumferential area, i.e.

it exhibits the adjacent cracked surface in the specimen gauge section. Again the mode of IGSCC predominates, and additional cracks appear on the side surface. On the other hand, at a potential that exceeds the passive potential range (e.g., +441 mV), the fracture surface has lost much of its intergranular character, as shown in figure 6.

At the corrosion potential of aluminum brass, intergranular cracking was completely absent and, instead, a typical dimpled structure was observed, at as shown in figure 7. It clearly shows that the failure mode for aluminum brass is predominantly ductile dimpled tearing fracture.

4. Discussion

A significant result of this study is that aluminum brass is extremely susceptible to SCC in the presence of fluoride at ambient temperature (~25℃). This SCC susceptibility was confirmed by the short failure time (2h in 0.1N NaF) at the slow strain rate of $3.8 \times 10^{-6} s^{-1}$. The failure time depended upon the applied electrochemical potential and the F^- ion content of the environment. However, the fracture mode of ductile dimpled rupture for aluminum brass is due to the absence of the active-passive behavior and the fact that the anodic current density consistently increases with time.

A clear relationship between the stress ratio and the anodic polarization potential of aluminum bronze was established. A sharp decrease of the stress ratio (σ_R) occurs for aluminum bronze at potentials between +341 mV and +391 mV, corresponding to the passive range of potentials identified in the potentiodynamic polarization curve. The potential range for cracking also corresponds to the potential range for Cu_2O stability, according to the potential-pH diagram [5] for Cu/H_2O at 25℃. A comparison of rapid and slow sweeps of the potential can indicate the range of potentials within which SCC is likely to occur [22]. That is to say, slower polarization with a longer time at each potentiodynamic step results in a lower current density at all potentials of the anodic polarization curve, especially in the passive region.

The local film breakdown at the applied potential of +391 mV (figure 5(b)) can be interpreted as resulting from the passive/pitting transition under tensile stress. In general, the SCC susceptibility of iron base alloys such as carbon steels and stainless steels in some special conditions appears to be greatest at the two extremes of the passive range potentials where the passive film is less stable and relatively weak [23], specifically, at the active/passive and the passive/pitting transitions. However, these two transitions, which SCC may occur readily, are not observed for aluminum bronze in 0.1N NaF (pH 6) at 25℃. In this study, the SCC susceptibility of aluminum bronze in fluoride solutions starts to increase significantly through the whole passive potential range. This may be attributed to the fact that fluoride ions can destroy the passive Cu_2O film on the aluminum bronze locally by forming specks of $AlF_3 \cdot 3H_2O$, which eventually lead to the passive film unstable even at the passive potential range. As indicated in figure 8(a), the existence of Cu_2O, $AlF_3 \cdot 3H_2O$ can be detected by XRD. The signals for Cu_2O are strong at 2θ values of 36.4° and 61.3°, corresponding to the crystallographic planes of (111) and (220), respectively; and the peaks for $AlF_3 \cdot 3H_2O$ occur at 2θ values of 16.2° and 23.1°, corresponding to (110) and (200), respectively. Furthermore, another corrosion product, which precipitated from the solution after long immersion times exhibited a bright blue color. X-ray diffraction data, as shown in figure 8(b), suggest it is CuF_2. The SCC is promoted by the rupture of the passive film leading to an accelerated dissolution at the slip steps because of the moving dislocations emerging at the specimen's surface during continuous straining [13].

The results were confirmed by the SEM observations on the fractured surface whereby a large number of cracks exist along the cylindrical surface close to the fracture, as shown in figure 5(c). It can be concluded that aluminum bronze suffers IGSCC due to the film-rupture mechanism [24], wherein SCC is promoted through the rupture of the passive film because of continuous strain.

Figure 9 shows the general attack and the X-ray mapping of Al and Zn on aluminum brass after anodic polarization. It is apparent that aluminum dissolves first to enrich the Zn content, which subsequently is de-zincified. The preferential dissolution of aluminum is likely to be attributable to the more active potential of Al (-1.662V) than Zn (-0.763V). Because Al and Zn are both strongly active to Cu (+0.337V), Al will first dissolve, after which Zn readily leaches out of the aluminum brass, leaving behind a relatively porous copper with poor mechanical strength. The favored leaching sites, such as grain boundaries, are also the favored paths for the propagation of cracks [10] and may serve as the initiation sites for SCC.

The potential-pH diagrams for Cu-H_2O, Al-H_2O and Zn-H_2O at 25℃ are superimposed in figure 10 assuming that all of the ionic activities (molality × activity coefficient) are 10^{-6} M. A potential de-alloying region is seen within the pH range 6-7 where Cu exists as Cu_2O, Zn as Zn^{2+} and Al as AlO_2^- at the corrosion potential of aluminum brass, ~ 241 mV (shown as an error bar in figure 10). The corresponding corrosion reaction of copper due to the direct complexing of copper by the fluoride ions can be written as follows:

$$Cu + 2F^- \rightarrow CuF_2^- + e^- \quad (3)$$

The Cu_2O surface film is then formed by hydrolysis of the CuF_2^- complex:

$$2CuF_2^- + H_2O \rightarrow Cu_2O + 4F^- + 2H^+ \quad (4)$$

Aluminum dissolves first by selective dissolution from aluminum brass as follows:

$$Al + 2H_2O \rightarrow AlO_2^- + 4H^+ + 3e^- \quad (5)$$

Zinc then dissolves by dezincification from aluminum brass as follows:

$$Zn \rightarrow Zn^{2+} + 2e^- \quad (6)$$

Since no signal for the fluoride compound was seen in the XRD pattern [25], it may be assumed that fluoride ions attack the aluminum brass through the combination with AlO^{2-} to form acids and oxides (e.g. Al_2O_3) [26], and with Zn^{2+} to form soluble complexes [11, 27]. Therefore, the increase of fluoride concentration increases the corrosion rate of aluminum brass, and thus stimulates the susceptibility to SCC. This implies that the stress enhances the anodic dissolution at the grain boundaries of the aluminum brass, and also that the F^- ions serve as a catalyst to accelerate the preferential dissolution of aluminum and zinc, thereby producing a de-alloyed layer on the aluminum brass. These reactions can be described as follows:

$$2Al + 3H_2O + 6F^- \rightarrow Al_2O_3 + 6HF + 6e^- \quad (7)$$

$$Al_2O_3 + H_2O + 6HF \rightarrow 2AlO_2^- + 8H^+ + 6F^- \quad (8)$$

$$Zn + 2F^- \rightarrow ZnF_2 + 2e^- \quad (9)$$

$$ZnF_2 \rightarrow Zn^{2+} + 2F^- \quad (10)$$

The pH values (6-7) considered above are, in fact, the values of the bulk solution. However, the surface pH of the system is perhaps slightly higher than that of the bulk because OH^- is always produced as a result of the cathodic reaction, i.e., either in the deaerated ($2H_2O + e^- \rightarrow 2OH^- + H_2$) or in the aerated ($2H_2O + O_2 + 4e^- \rightarrow 4OH^-$) water. As indicated in figure 10, at a surface pH≥8.5, Zn would appear as $Zn(OH)_2$, which was, in fact, also observed on the surface of the specimen and

detected by EPMA. In this study, the boundaries in the superimposed potential-pH diagram assume that the activities of all possible chemical species are 10^{-6} M. On the assumption that $11 \geq pH \geq 8.5$ at the corrosion potential of 0.241 V where Cu exists as Cu_2O, Zn as $Zn(OH)_2$ and Al as AlO_2^-, the allowable ionic activities observed from the Pourbaix diagrams [5] at 25℃ are $10^{-6}M \geq (Cu^{2+}) \geq 10^{-8}M$, $10^{-6}M \geq (Zn^{2+}) \geq 10^{-7}M$ and $10^{-4}M \geq (AlO_2^-) \geq 10^{-6}M$.

In order to facilitate the analysis of the corrosion potential (E_{corr}), it is necessary to compare the corrosion potentials for the two copper alloys with the equilibrium potential for oxygen reduction as a consequence of the aeration of the NaF solution. Thus, at pH 7 (25℃), the equilibrium potential for $1/2O_2$ (0.21atm) + H_2O + $2e^-$ = $2OH^-$ (pH=7) is +0.804 V; this potential (E_c) is noble to the corrosion potentials of both aluminum brass (+0.241 V) and aluminum bronze (+0.191 V). On the other hand, the equilibrium potential for the anodic dissolution (E_a) was also calculated; for instance, assuming the following parameters for aluminum brass and the activities of all possible chemical species are 10^{-6} M:

$$E_{a,Cu/Cu2O} = 0.471 - 0.0591pH = 0.0573V$$
$$E_{a,Zn/Zn(OH)2} = -0.439 - 0.0591pH = -0.8527V$$
$$E_{a,Al/AlO2-} = -1.262 - 0.0788pH + 0.0197\log(AlO_2^-) = -1.9515V$$

The micro-galvanic cell effect of each compositional element on the galvanic potential (E_a) for aluminum brass can be determined by adding the weighted values. This had done by multiplying the atomic percentage by the individual equilibrium anodic potential, then adding these weighted values together to approximate the alloy's anodic equilibrium potential. Consequently, the composite anodic potential of aluminum brass or the galvanic potential of Cu, Zn, and Al is 0.0573V ×74.65 at% + (-0.8527V) ×21.19 at% + (-1.9515V) ×4.16 at% = -0.218V. Similarly, the composite anodic potential for aluminum bronze is -0.203V. These two equilibrium potentials are more active than the corrosion potential (E_{corr}) for the two copper alloys. Hence, the corrosion potentials measured in the aerated NaF solution are consistent with the thermodynamic necessity that they always lie between the equilibrium anodic and cathodic potentials, as shown in figure 11. In view of the influence of polarization on the corrosion rate, corrosion at pH 6-7 for the both alloys is under mixed control; in that polarization occurs to some degree at both anodes and cathodes (E_{corr} is roughly halfway between E_a and E_c).

The stress ratio and time-to-fracture ratio of the aluminum brass decreases markedly as the concentration of the anion, F^-, increases. A logarithmic relation is established for the system in question: $R = -m \log [F^-] + n$, where R is either stress ratio or time-to-fracture ratio. It is seen that an increasing F^- concentration reduces the two ratios significantly. The presence of the adsorbed fluoride ions on the metal surface retards the growth of the passive film and thus allows the establishment of active pits. The value, m, depends on the alloy system, the solution type [28, 29], and the electrochemical technique used [30]. However, the characteristics of the stress ratio and time-to-fracture ratio as a function of F^- concentration have not been reported in the literature.

5. Conclusions

The susceptibility of the two copper-based alloys to SCC was observed in the presence of sodium fluoride solutions using the SSRT. Aluminum brass suffers SCC even at the corrosion potential. A local de-alloying mechanism is responsible for such cracking. In addition, both the stress ratio (σ_R) and the time-to-fracture ratio (t_f) depend on the concentration of F^-

according to the equation: $R = -m \log [F^-] + n$.

In contrast, aluminum bronze does not exhibit SCC susceptibility under similar conditions. However, the susceptibility for SCC of aluminum bronze can be predicted from a comparison of anodic polarization curves generated at fast (1 V/min) and slow (20 mV/min) scan rates. SCC can be promoted by applying an anodic potential in the passive region where oxide films prevail. A film-rupture mechanism is therefore accountable for the failure of aluminum bronze observed in fluoride environments.

The micro-galvanic cell approach can be used to estimate the anodic equilibrium potential of the alloy by multiplying the atomic percentage of each compositional element by the individual equilibrium anodic potential, and then adding these weighted values together.

References

1. R. N. Parkins, Corros. Sci., 20 (1980) 147.
2. J. G. Parker and W. C. Pearce, Corrosion, 30 (1974) 18.
3. R. N. Parkins and N. J. H. Holroyd, Corrosion, 38 (1982) 245.
4. V. K. Gouda, H. A. El-Syaed, and G. M. Sherbini, Br. Corros. J., 18 (1983) 40.
5. M. Pourbaix, in：*Atlas of electrochemical equilibria in aqueous solution,* Pergamon press, London, (1974), p.171, 387, and 409.
6. S. Torchio, Corros. Sci., 21 (1981) 425.
7. F. Mazza and S. Torchio, Corros. Sci., 23 (1983) 1053.
8. S. Torchio, Corros. Sci., 21 (1981) 59.
9. J. E. Finnegan, R. E. Hummel, and E. D. Verink, Jr., Corrosion, 37 (1981) 256.
10. E. D. Verink and P. A. Parrish, Corrosion, 26 (1970) 214.
11. H. C. Shih, R. J. Tzou, Y. N. Chen, and Y. S. Lee, Corrosion, 45 (1990) 913.
12. H. C. Shih and R. J. Tzou, Corros. Sci., 35 (1993) 479.
13. H. C. Shih and R. J. Tzou, International Conference on Environment-Induced Cracking of Metals, Kohler, Wisconsin, USA, October 2-7, 1989, pp. 389-395.
14. C. K. Lee and H. C. Shih, J. Electrochem. Soc., 142 (1995) 731.
15. ASTM G49-85, Annual Book of ASTM Standards, Philadelphia, PA, 1982.
16. J. Congleton, H. C. Shih, T. Shoji, and R. N. Parkins, Corros. Sci., 25 (1985) 769.
17. S. A. Bradford and T. Lee, Corrosion, 34 (1978) 96.
18. S. S. Birley and D. Tromans, Met. Trans., 12A (1981) 1215.
19. J. Yu, N. J. H. Holroyd, and R. N. Prakins, in: Environment-Sensitive Fracture: *Evaluation and Comparison of Test Methods,* ASTM STP 821 (1982) p.288.
20. ASTM G5-82, Annual Book of ASTM Standards, Philadelphia, PA, 1982.
21. D. A. Jones, in：*Principles and Prevention of Corrosion,* 2nd Edition, Prentice Hall, NJ (1996), 66.
22. R. N. Parkins, N. J. H. Holroyd, and R.R. Fessler, Corrosion, 34 (1978) 253.
23. D. A. Jones, in：Principles and Prevention of Corrosion, 2nd Edition, Prentice Hall, NJ (1996), 239.
24. N. R. Smart, P. M. Scott, and R. P. M. Procter, Corros. Sci., 30 (1990) 877.
25. J. C. Oung, C. K. Lee, and H. C. Shih, Corros. Prevent. Control, August (1997) 106.
26. T. Valand and G. Nilsson, Corros. Sci., 17 (1977) 449.
27. H. C. Shih and R. J. Tzou, J. Electrochem. Soc.,

138 (1991) 985.
28. H. H. Strehblow and B. Title, Corros. Sci., 17 (1977) 461.
29. G. Matamala, Corrosion, 43 (1987) 97.
30. R. Fratesi, Corrosion, 41 (1985) 114.

收到日期：2004 年 7 月 10 日
修訂日期：2005 年 2 月 15 日
接受日期：2005 年 3 月 18 日

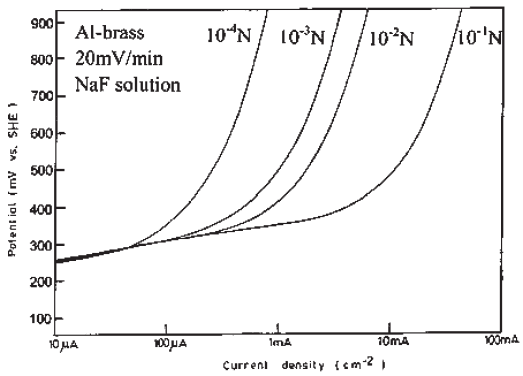

Figure 1 Effects of fluoride concentrations on the anodic potentiodynamic polarization curves of aluminum brass in various concentrations of the NaF solution.

圖1 鋁黃銅在不同濃度的氟化鈉溶液中，氟離子濃度對其動態陽極極化曲線的影響。

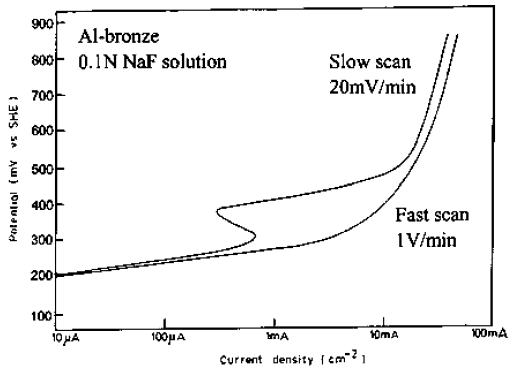

Figure 2 Effects of fast and slow scan rates on the anodic potentiodynamic polarization of aluminum bronze in 0.1N NaF solution.

圖2 鋁青銅在 0.1N 氟化鈉溶液中，極化掃瞄速率的快與慢對其動態極化曲線的影響。

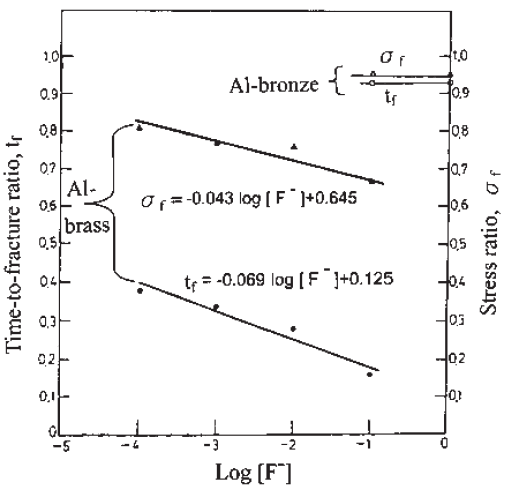

Figure 3 Effect of fluoride concentration (N) on the SCC susceptibility of (a) aluminum brass, and (b) aluminum bronze at their open circuit potentials.

圖3 氟離子濃度(當量濃度)對 (a) 鋁黃銅和 (b) 鋁青銅在其開路電位時的應力腐蝕敏感度的影響。

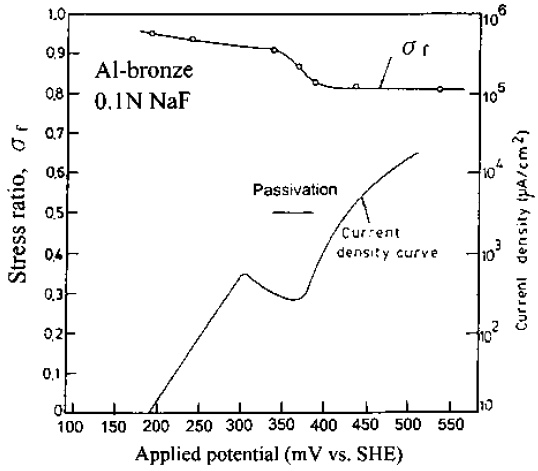

Figure 4 Effect of applied potential on SSRT data of aluminum bronze in 0.1N NaF (pH = 6, 25 ℃).

圖4 外加電位對鋁青銅在 0.1N 的氟化鈉 (pH = 6, 25℃) 中之慢速應變拉伸數據的影響。

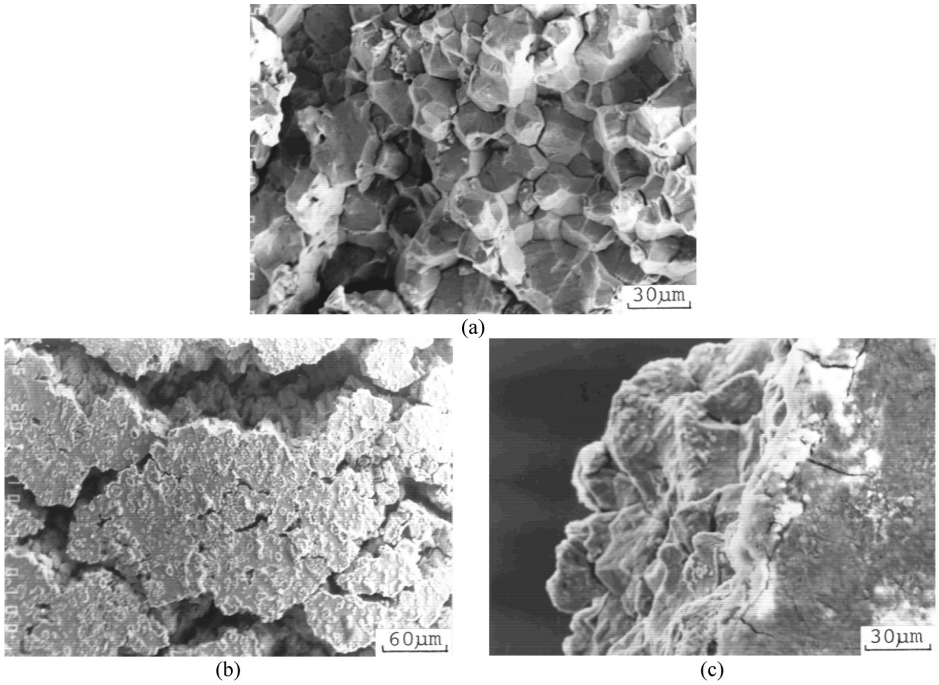

Figure 5 Aluminum bronze under the applied potential of +391 mV in 0.1N NaF solution: (a) IGSCC of aluminum bronze (b) Pits and secondary cracks of aluminum bronze. The tensile direction is perpendicular to the secondary cracks in this figure, and (c) Film rupture and IGSCC of aluminum bronze.

圖5　(a) 鋁青銅在 0.1N 的氟化鈉溶液中，於 +391 mV 的外加電位下會產生沿晶應力腐蝕破裂的情形，(b) 於 +391 mV 的外加電位下會產生孔洞與二次裂痕的情形。此圖的拉伸方向垂直於二次裂痕，及 (c) 於 +391 mV 的外加電位下會有鈍態膜剝落和沿晶應力腐蝕破裂的情形。

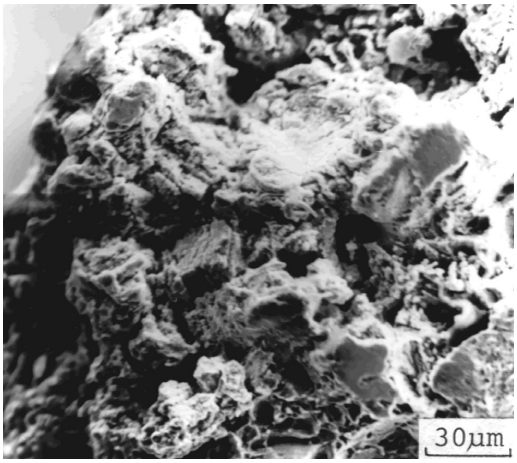

Figure 6 Fractured surface of aluminum bronze at +441 mV applied potential in 0.1N NaF solution.

圖6　鋁青銅在 0.1N 的氟化鈉溶液中，於 +441 mV 的外加電位下之破裂表面。

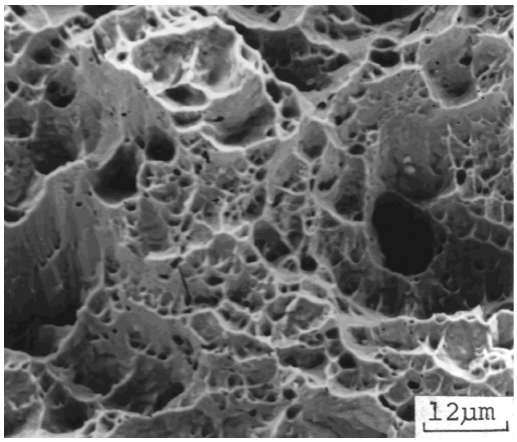

Figure 7 Ductile dimpled tearing rupture of aluminum brass in 0.1N NaF solution at the corrosion potential (+0.241 mV).

圖7 鋁黃銅在 0.1N 的氟化鈉溶液中，於其腐蝕電位 (+0.241 mV) 時會產生延性撕裂狀的窩穴。

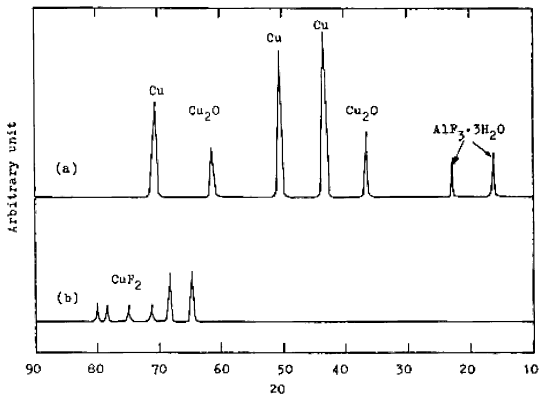

Figure 8 X-ray diffraction pattern of the corroded specimen of aluminum bronze in 0.1N NaF (pH 6) at 25 ℃.

圖8 鋁青銅在 0.1N 的氟化鈉 (pH = 6, 25℃) 中腐蝕過後，試片的 X 光繞射圖譜。

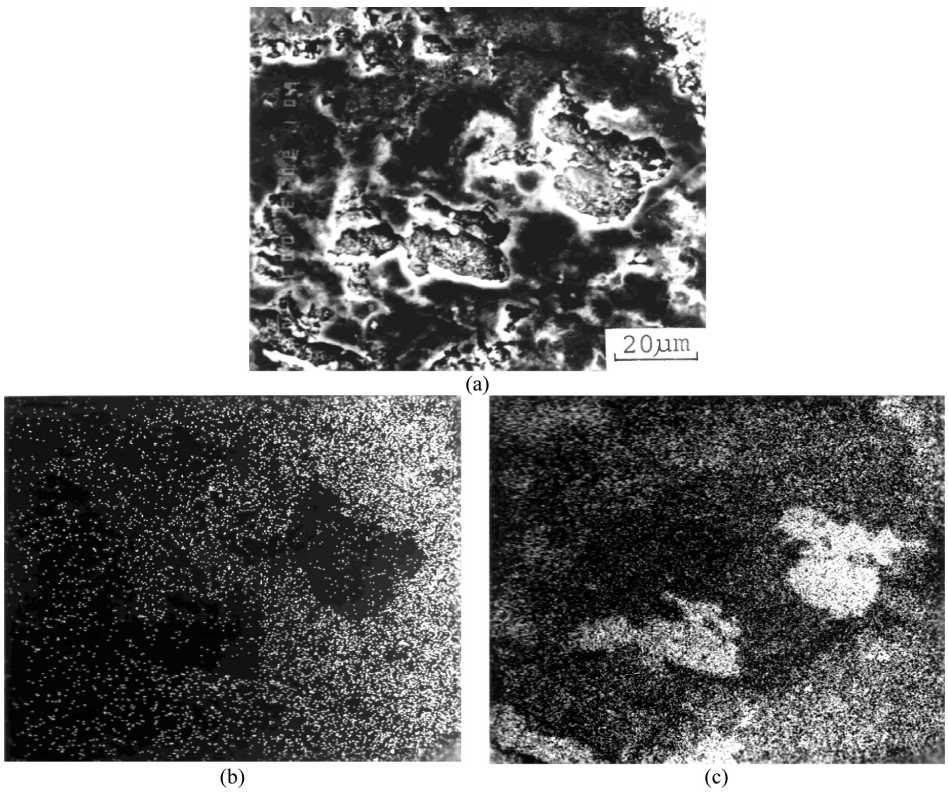

Figure 9 (a) General corrosion of aluminum brass in 0.1N NaF solution after the anodic polarization, (b) X-ray mapping of aluminum, and (c) X-ray mapping of zinc.

圖9 (a) 鋁黃銅在 0.1N 的氟化鈉溶液中，在陽極極化後所產生的均勻腐蝕，(b) 鋁的 X 光映像，及(c) 鋅的 X 光映像。

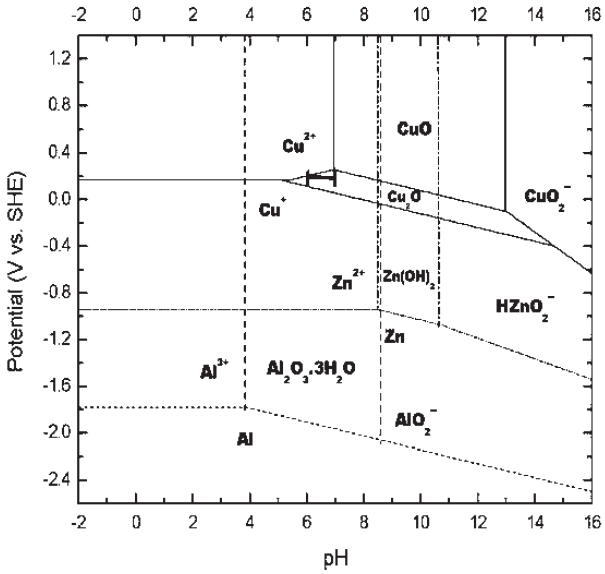

Figure 10 Superimposition of the potential-pH diagrams for Cu-H_2O, Al-H_2O, and Zn-H_2O, indicating the possible chemical species that exist when de-alloying mechanism takes place. Assumes the activities of all possible chemical species are 10^{-6}M.

圖10　從銅-水、鋁-水和鋅-水三種電位與 pH 值關係圖的加成圖中顯示出去合金機制發生時可能存在的化學種類。在這裡我們假設所有可能的化學種類 (離子或氣體) 其活度均為 10^{-6} M。

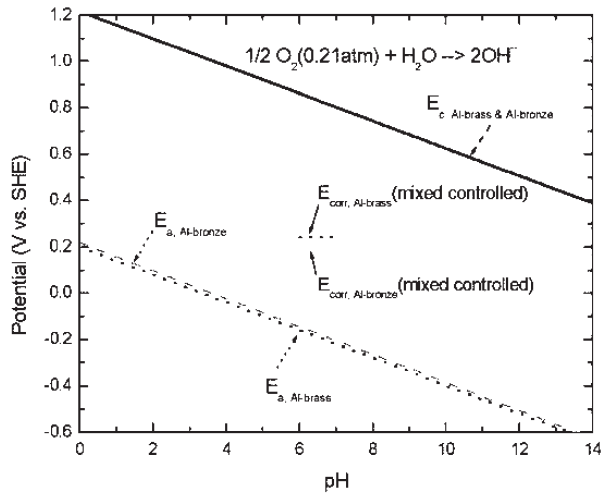

Figure 11 Comparison of the E_{corr} of both aluminum brass and aluminum bronze with their anodic (E_a) and cathodic (E_c) equilibrium potentials at various pH values (25℃).

圖11　鋁黃銅與鋁青銅其腐蝕電位與陽極、陰極平衡電位在不同 pH 值 (25℃) 時的比較。